

RL-TR-97-124
In-House Report
OCTOBER 1997



NUMERICAL SIMULATIONS OF SCATTERING IN A TWO-PHOTON OPTICAL DATA STORAGE SYSTEM

Joshua L. Kann

19980311 038

APPROVED FOR PUBLIC RELEASE; DISTRIBUTION UNLIMITED.

DTIC QUALITY INSPECTED 4

**Rome Laboratory
Air Force Materiel Command
Rome, New York**

Although this report references limited documents(*), listed on page 26, no limited information has been extracted.

This report has been reviewed by the Rome Laboratory Public Affairs Office (PA) and is releasable to the National Technical Information Service (NTIS). At NTIS it will be releasable to the general public, including foreign nations.

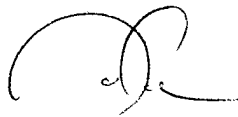
RL-TR-97-124 has been reviewed and is approved for publication.

APPROVED:



RONALD W. CWIRKO
Chief, Signal Intelligence Division
Intelligence & Reconnaissance Directorate

FOR THE DIRECTOR:



JOSEPH CAMERA, Technical Director
Intelligence & Reconnaissance Directorate

If your address has changed or if you wish to be removed from the Rome Laboratory mailing list, or if the addressee is no longer employed by your organization, please notify Rome Laboratory/IRAP, Rome, NY 13441. This will assist us in maintaining a current mailing list.

Do not return copies of this report unless contractual obligations or notices on a specific document require that it be returned.

REPORT DOCUMENTATION PAGE

Form Approved
OMB No. 0704-0188

Public reporting burden for this collection of information is estimated to average 1 hour per response, including the time for reviewing instructions, searching existing data sources, gathering and maintaining the data needed, and completing and reviewing the collection of information. Send comments regarding this burden estimate or any other aspect of this collection of information, including suggestions for reducing this burden, to Washington Headquarters Services, Directorate for Information Operations and Reports, 1215 Jefferson Davis Highway, Suite 1204, Arlington, VA 22202-4302, and to the Office of Management and Budget, Paperwork Reduction Project (0704-0188), Washington, DC 20503.

1. AGENCY USE ONLY (Leave blank)		2. REPORT DATE October 1997	3. REPORT TYPE AND DATES COVERED In House 1 May 96 - 1 May 97	
4. TITLE AND SUBTITLE NUMERICAL SIMULATIONS OF SCATTERING IN A TWO-PHOTON OPTICAL DATA STORAGE SYSTEM			5. FUNDING NUMBERS PE - 62702F PR - 4594 TA - 15 WU- P8	
6. AUTHOR(S) Joshua L. Kann				
7. PERFORMING ORGANIZATION NAME(S) AND ADDRESS(ES) Rome Laboratory/IRAP 32 Hangar Road Rome, NY 13441-4514			8. PERFORMING ORGANIZATION REPORT NUMBER RL-TR-97-124	
9. SPONSORING/MONITORING AGENCY NAME(S) AND ADDRESS(ES) Rome Laboratory/IRAP 32 Hangar Road Rome, NY 13441-4514			10. SPONSORING/MONITORING AGENCY REPORT NUMBER RL-TR-97-124	
11. SUPPLEMENTARY NOTES Rome Laboratory Project Engineer: Joshua Kann/IRAP, (315)330-2369				
12a. DISTRIBUTION AVAILABILITY STATEMENT Approved for public release; distribution unlimited.			12b. DISTRIBUTION CODE	
13. ABSTRACT (Maximum 200 words) Scattering effects in a two-photon optical data storage system are numerically studied. Surface scattering analysis using a scalar, beam propagation model is performed. The problem is analyzed by computing scattering from randomly varying surfaces, and also by Fourier surface decomposition. Scattering induced by propagation through pages of randomly recorded data marks is also studied using a hybrid finite-difference-time-domain/angular spectrum model. Both surface and bulk scattering are shown to influence the spatial properties of the optical beam. Results and some possible implications are presented.				
14. SUBJECT TERMS two-photon optical memory, beam scattering, vector diffraction			15. NUMBER OF PAGES 32	
			16. PRICE CODE	
17. SECURITY CLASSIFICATION OF REPORT UNCLASSIFIED	18. SECURITY CLASSIFICATION OF THIS PAGE UNCLASSIFIED	19. SECURITY CLASSIFICATION OF ABSTRACT UNCLASSIFIED	20. LIMITATION OF ABSTRACT UL	

TABLE OF CONTENTS

1.0 INTRODUCTION	3
1.1 TWO-PHOTON OPTICAL DATA STORAGE SYSTEMS	3
1.2 THE SCATTERING PROBLEM	6
2.0 SURFACE SCATTERING EFFECTS	6
2.1 NUMERICAL MODEL	7
2.2 SCATTERING FROM RANDOM SURFACES	8
2.3 SPATIAL FREQUENCY ANALYSIS	11
3.0 SCATTERING FROM PREVIOUSLY WRITTEN DATA MARKS	19
3.1 NUMERICAL MODEL	19
3.2 RESULTS	20
4.0 SUMMARY AND CONCLUSIONS	25
5.0 REFERENCES	26

1.0 Introduction

As modern day computing systems continue to advance, it is apparent that for many applications the ultimate capability of the system may be limited by memory (either primary, secondary or tertiary) performance parameters and not the computer's processing power or speed. Thus, the need for high capacity, fast data transfer rate (I/O) storage systems becomes critical in areas such as image storage and analysis and digital video servers. Optical data storage systems are very promising due to the potential for ultra-high storage densities and parallel I/O [1]. Currently, state of the art two-dimensional optical data storage disc systems (such as DVD) have capacities of 4.7 GB, with near-term expansion to 17 GB, and throughput rates of 10 Mb/s [2]. Unfortunately, these systems record data on only one or two planes and are sequential in nature. The next logical step in achieving orders of magnitude increase in capacity and throughput rates is expected to involve some form of a three-dimensional, parallel access memory.

By definition, a three-dimensional memory is a single memory unit where three independent coordinates specify the location of stored information. By storing information in volumetric media, very high densities ($\sim 1 \text{ Tb/cm}^3$) can be achieved. In three-dimensional memories, read, write and erase operations are performed on the entire bit plane, giving rise to a tremendous data capacity increase over conventional two-dimensional bit-oriented memories. Through the inherently parallel nature of data manipulation, high-speed reading and writing of an entire memory plane becomes feasible. These considerations make three-dimensional memories very compatible with emerging, highly integrated parallel array processors and optoelectronic multiprocessors. Three-dimensional memory systems include two-photon absorption, holographic and spectral-hole burning. In this report, numerical models are used to study beam propagation effects in a two-photon absorption based memory.

1.1 Two-photon optical data storage systems

The basic premise of a two-photon recording system is the simultaneous absorption of two photons whose combined energy is equal to the energy difference between the initial and final states of the recording material [3-5]. This simultaneous absorption results in a change in the molecular structure of the material. This structural change alters various properties of the material, including index of refraction, the absorption spectrum and the fluorescence spectrum. Therefore, by intersecting two optical beams, spatially and temporally, the material's optical properties can be altered locally and are addressable anywhere within a three-dimensional space. Digital data is written in this fashion, with the ultimate limitation on storage capacity set by diffraction effects in the optical system. Data readout is accomplished by probing the material with a single read beam to measure a change in one of the material's optical properties.

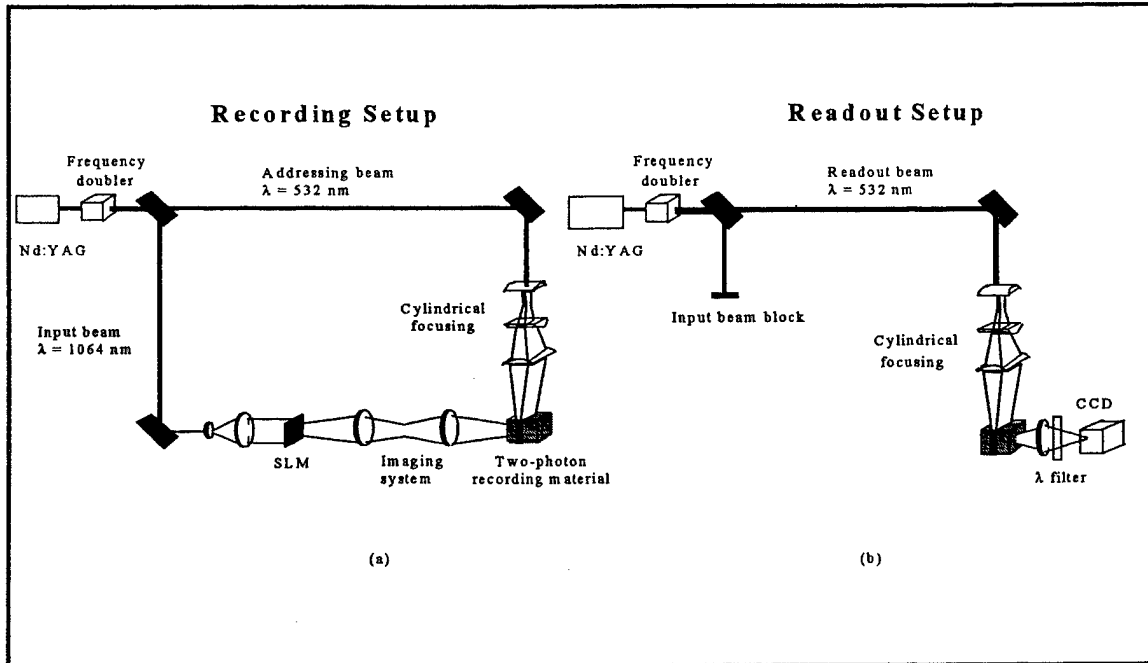


Figure 1 The recording (a) and readout (b) systems used for a two-photon memory.

Rome Laboratory is currently working with Call/Recall, Inc. in San Diego, California to develop this technology. A schematic of the current Read Only Memory (ROM) system architecture is shown in Fig. 1. The system uses picosecond pulses of the first and second harmonic ($\lambda_1 = 1064 \text{ nm}$, $\lambda_2 = 532 \text{ nm}$) of a Nd:YAG laser. Data recording is shown in Fig. 1(a), while data retrieval (readout) is shown in Fig. 1(b). Digital information is recorded in the two-photon material as pages of digital data, the data planes separated in the axial (z) direction. The input (data) arm of the system ($\lambda = 1064 \text{ nm}$) is spatially modulated with a Spatial Light Modulator (SLM) and imaged to the proper plane within the cube. A second, addressing beam ($\lambda = 532 \text{ nm}$), propagating orthogonal to the input beam, is cylindrically focused throughout the cube. A page of data is recorded when the input beam and addressing beam simultaneously illuminate the image plane. The axial resolution is limited by the divergence of the addressing beam, while the lateral resolution is determined by diffraction effects and aberrations in the input arm. Readout is accomplished by measuring the fluorescence of the material. The input beam is blocked and the 532 nm beam is cylindrically focused to read the proper data page. For the unwritten material, the 532 nm beam is unabsorbed and passes through the system. However, for the written form of the material, the readout beam is absorbed, exciting a fluorescence at a longer wavelength. The readout plane is then imaged through a wavelength selective filter onto a Charge Coupled Device (CCD). Thresholding of the individual pixels of the CCD is performed to digitize the data.

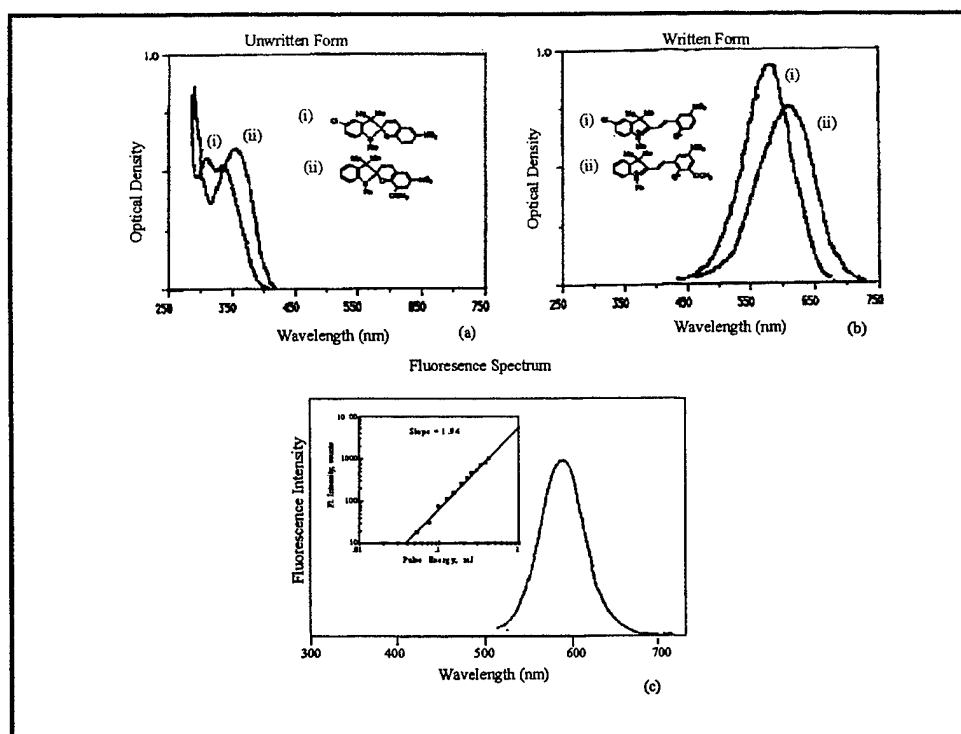


Figure 2 The absorption (a-b) and fluorescence (c) spectrum for two different types of SP compositions.

A variety of recording materials have been proposed. The proper material must possess several key characteristics in order to be considered. These characteristics include: photocromism (the change of chemical structure after excitation by light), a fluorescence in one of the two chemical states, stability of both states at room temperature, ability to read data 10^6 times without loss of information, high quantum efficiency of the read form fluorescence, and a wide enough wavelength shift between the read beam and peak of the fluorescence spectrum to prevent cross-talk. One of the more promising candidates, Spirobenzopyran (SP) is discussed in the following paragraph.

Spirobenzopyran molecules are composed of two distinct molecular components linked by a sp^3 hybridized carbon. Simultaneous absorption of a 532 nm photon and a 1064 nm photon alters the chemical state of the material, as shown by the absorption spectra in Figs. 2(a) and 2(b). (In Figs. 2(a) and 2(b), the absorption spectra of two different species of the material, (i) and (ii), are shown.) The unwritten form, Fig. 2(a), is colorless in appearance and shows strong absorption in the ultraviolet ($\lambda < 400$ nm) portion of the spectrum. However, the written form, Fig. 2(b), is colored in appearance and shows strong absorption in the 550 nm spectral region. Transitioning between these two molecular states results in localized changes in the optical properties of the material, including index of refraction (real and imaginary part) and the fluorescence spectrum. The fluorescence spectra of SP, shown in Fig 2(c), is peaked around 600 nm. This peak is sufficiently separated from the read wavelength to prevent cross-talk during readout. To fabricate solid, stable recording materials, the SP is dispersed in polymers such as PMMA.

1.2 The scattering problem

As mentioned earlier, the diffraction limited spot size can yield potential data densities of 1 Tb/cm³. However, optical aberrations and scattering effects will result in a re-distribution of the electric field (**E**) at the desired read/write location. This may result in lower data densities and slower read/write speeds due to a reduction in the beam quality and the peak optical power at the desired spatial location. Optical aberrations can be analyzed, and largely corrected, using ray-tracing techniques. Scattering effects, however, are more difficult to quantify. In this report, numerical models are used to analyze the effects of scattering in a two-photon system. Specifically, the problem is broken into two distinct parts: (1) scattering effects from the rough entrance surface of the storage media and (2) scattering from previously written planes of data marks. The first problem can be simulated using conventional scalar diffraction theory. The second problem, requires more complicated vector-based methods. In this report, a scalar-based angular-spectrum beam propagation method is used to quantify the effects of surface roughness. The results are presented in Section 2. A hybrid finite-difference-time-domain (FDTD)/angular spectrum approach is used to study the effects of scattering off of previously written pages of data. A description of the method and some results are presented in Section 3. Finally, a summary and relevant conclusions are presented in Section 4.

2.0 Surface scattering effects

Early experimental results have shown irradiance fluctuations in the recorded pages of data. It is believed that these fluctuations are caused by non-perfect, rough surfaces at the face of the material where the optical beam enters. Figure 3 shows a surface profilometry measurement made on one surface of an SP cube. The *x*-axis corresponds to the lateral direction, while the *z*-axis corresponds to the normal direction (height). Figure 3(b) is over a smaller range of *x*. It is assumed that the surface profile in the other transverse direction (*y*) is very similar. While these measurements will not be directly used in this work, they do give an order of magnitude estimate on the range of potential surface roughness. It is important to note that this cube's surface was fabricated using a polishing technique. Call/Recall is currently planning to transition to an injection molding process, and expects to see significantly smoother surfaces.

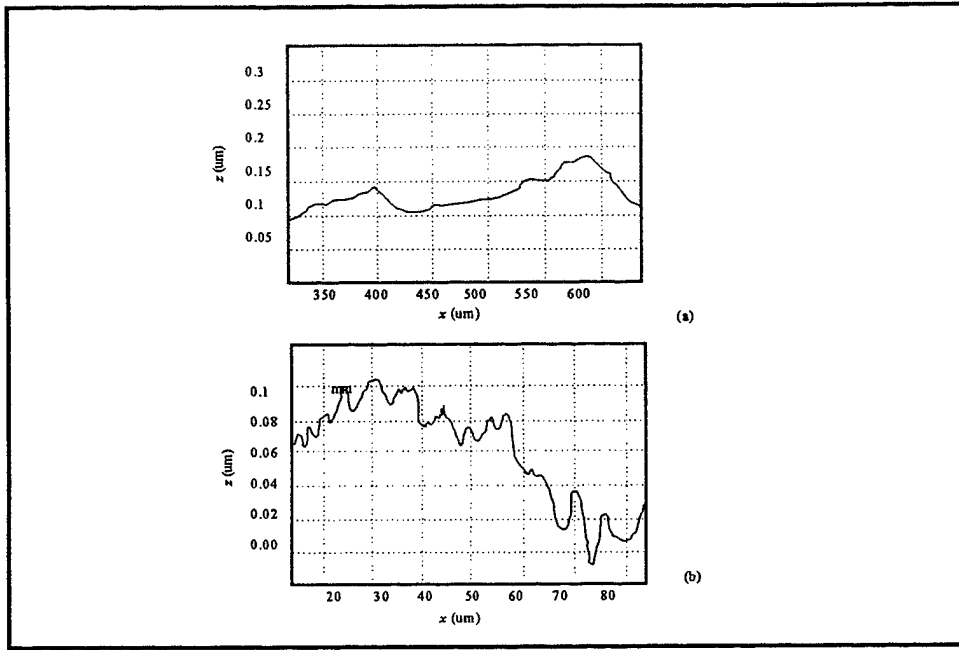


Figure 3 Surface measurement of SP recording material.

2.1 Numerical model

The model used in this section is designed to study and understand how the addressing beam is affected as it propagates through a rough surface. The field is assumed to be Gaussian in the x -direction with a beam waist defined by its $\text{FW1}/e^2$ value and collimated in the y -direction. In the y -direction, the beam also has a Gaussian profile, with a $\text{FW1}/e^2$ value of 8 mm. The $\text{FW1}/e^2$ value in the x -direction is related to the plane-to-plane spacing of data pages. The beam waist is 5 mm beyond the front surface of the cube, in the z -direction. The field is first computed at the waist, and then backwards propagated to the front surface of the cube. The complex-valued field at the surface is then multiplied by the transmittance function of the surface, given by:

$$t(x,y) = \exp\{-jkh(x,y)\}, \quad (1)$$

where $k=2\pi/\lambda$, and $h(x,y)$ is the surface height (deviation from the nominal height at each x,y location). After multiplication by $t(x,y)$, the beam is then re-propagated to the waist through the SP material (unwritten form). For each run, a nominal case is also performed, with a perfectly flat surface ($h(x,y) = 0$). For all of the work presented in this report, the wavelength, λ , is 500 nm. The surface is modeled as a purely phase perturbing structure with uniform amplitude transmittance. For simplicity, the program is broken up into two, two-dimensional problems assuming a separability of the field and transmittance in x and y . The code is written in MATLAB and runs on a PC.

2.2 Scattering from random surfaces

In this section, the cube's surface is modeled as a randomly varying surface. The value of $h(x,y)$ is found using MATLAB's random number generator (using a normal probability density function). The height is found by

$$\begin{aligned} h(x) &= \text{Gaus}(x/b_x) * \text{randnormal}(x, \sigma_x^2) \\ h(y) &= \text{Gaus}(y/b_y) * \text{randnormal}(y, \sigma_y^2), \end{aligned} \quad (2)$$

where the Gaus function is a Gaussian function defined by Gaskill [6], and randnormal indicates that a random number is chosen at each x (or y) location with a variance of σ_x^2 (σ_y^2). The function is then convolved with a Gaussian of width b_x (b_y in the y case) to provide smoothing (i.e. low pass filter $h(x)$ or $h(y)$.) Therefore, the value of σ_x^2 (σ_y^2) is related to the variance of the height, while the parameter b_x (b_y) determines how smoothly varying the surface is.

In Fig. 4, a computed surface profile is shown for the x direction. The parameters used for this plot are $\sigma_x^2 = \lambda/10$ and $b_x = 50 \mu\text{m}$.

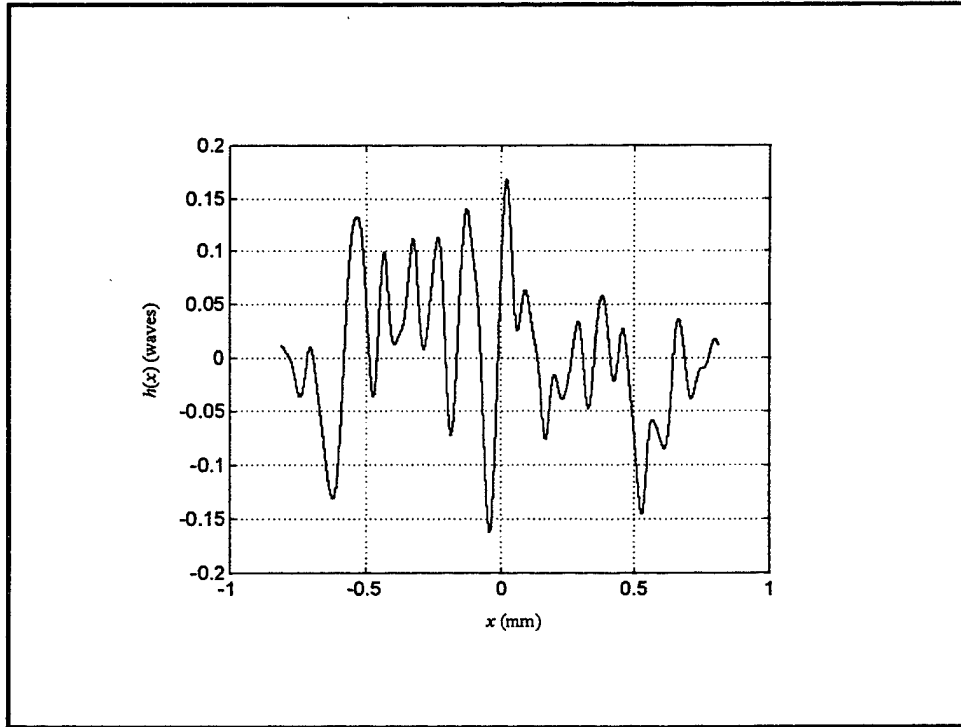


Figure 4 Computed surface profile in the x -direction. The value of $h(x)$ is normalized by the wavelength.

In Figs. 5(a) through (e), the field at the waist is shown for a beam waist $\text{FW}1/e^2$ (BW) values of $5 \mu\text{m}$, $10 \mu\text{m}$, $20 \mu\text{m}$, $40 \mu\text{m}$ and $80 \mu\text{m}$, respectively. For statistical purposes, three cases were run for each beam waist value, corresponding to three randomly chosen surfaces. The three cases are shown by the broken lines, while the solid line corresponds to the nominal case of a flat surface.

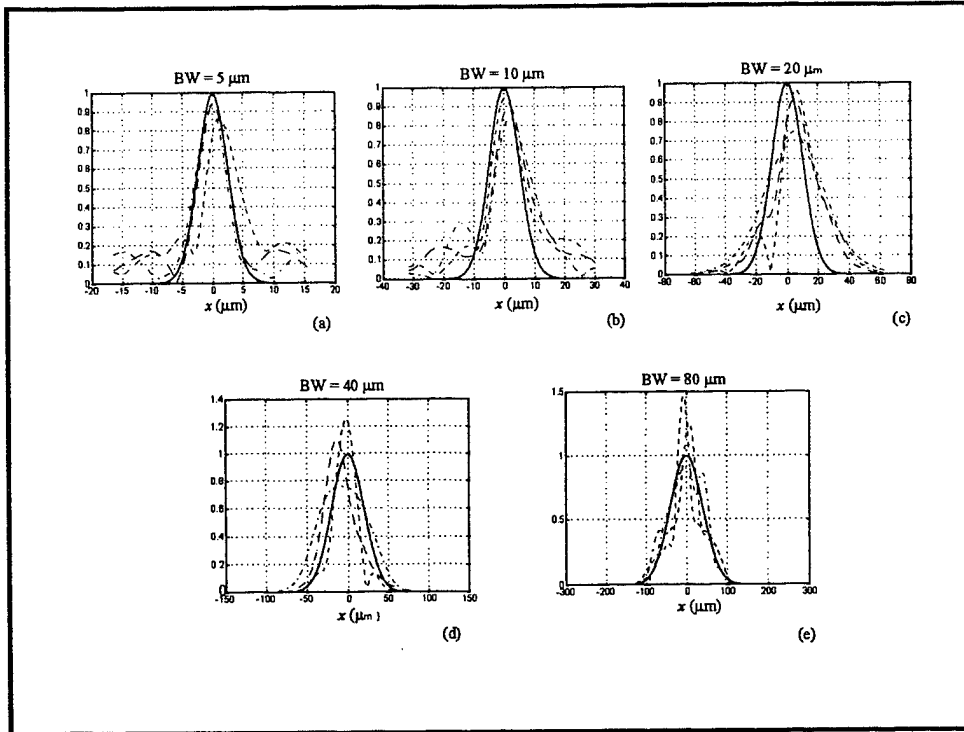


Figure 5 Beam profile at the beam waist when scattered off of a rough surface. The x profile is shown.

In examining Figs. 5(a) through (e), it is apparent that surface scattering plays a major role in both the spatial distribution of the field and also the centroid of the energy distribution. It seems that the effects become greater for larger beam waists. One possible explanation for this, is that the beam with a smaller waist diverges much more rapidly and, therefore, has a wider beam print at the front surface of the cube. For example at the entrance face of the cube, the $FW1/e^2$ is $333 \mu\text{m}$ when $BW = 5 \mu\text{m}$, but only $82.6 \mu\text{m}$ when $BW = 80 \mu\text{m}$. With a wider beam at the entrance surface of the cube, random variations in the surface are more likely to be averaged out.

In Figs. 6(a) through (d), the y -profile of the beam is shown with the surface parameter $b_y = 250 \mu\text{m}$. The value of σ_y^2 is changed in each plot. The values are $\lambda/2$, $\lambda/5$, $\lambda/10$ and $\lambda/25$ for (a) through (d), respectively.

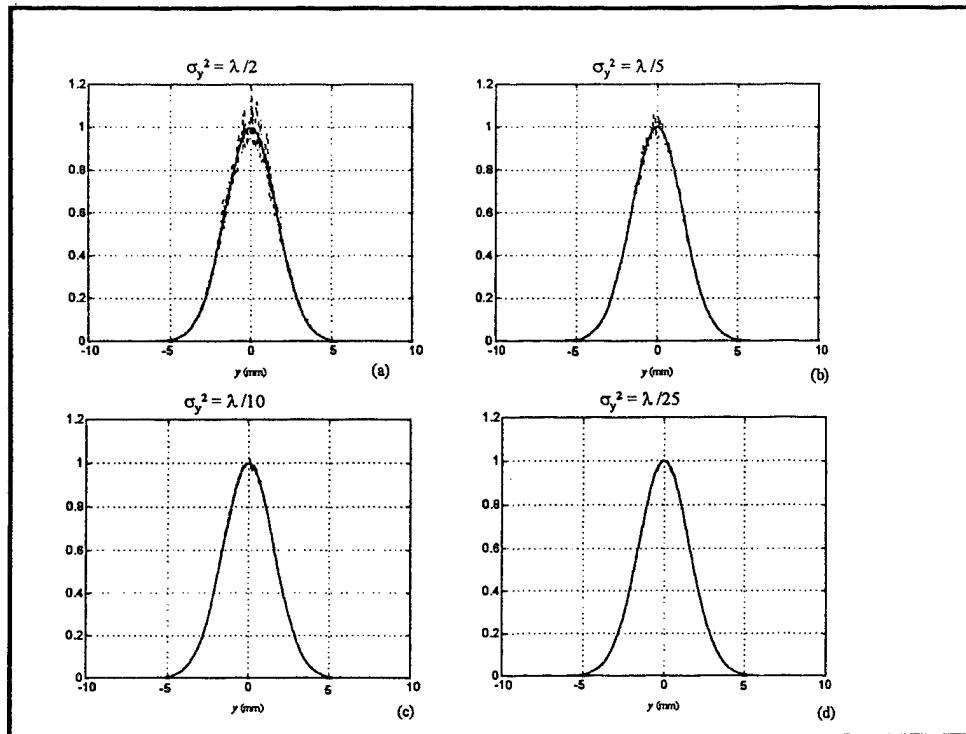


Figure 6 Beam profile at the beam waist when scattered off of a rough surface. The y profile is shown.

Again, it is clear that scattering plays a fairly substantial role in the beam quality, even in the collimated (non-focused) direction. For the y -direction, however, there is little shift in the centroid of the beam. For large surface variations, fairly significant oscillations (10-15% modulation) are observed around $y = 0$. This may be the cause of the irradiance variations observed experimentally.

In order to study the errors more quantitatively, the RMS error was calculated for seven different values of σ_y^2 . For each value of σ_y^2 , the computations described above were repeated for eight randomly chosen surface profiles $h(y)$. The bar chart in Fig. 7, shows the RMS error versus σ_y^2 . The solid line through the bar chart shows a line through the mean RMS error (in percentage) for each value of σ_y^2 (normalized by λ).

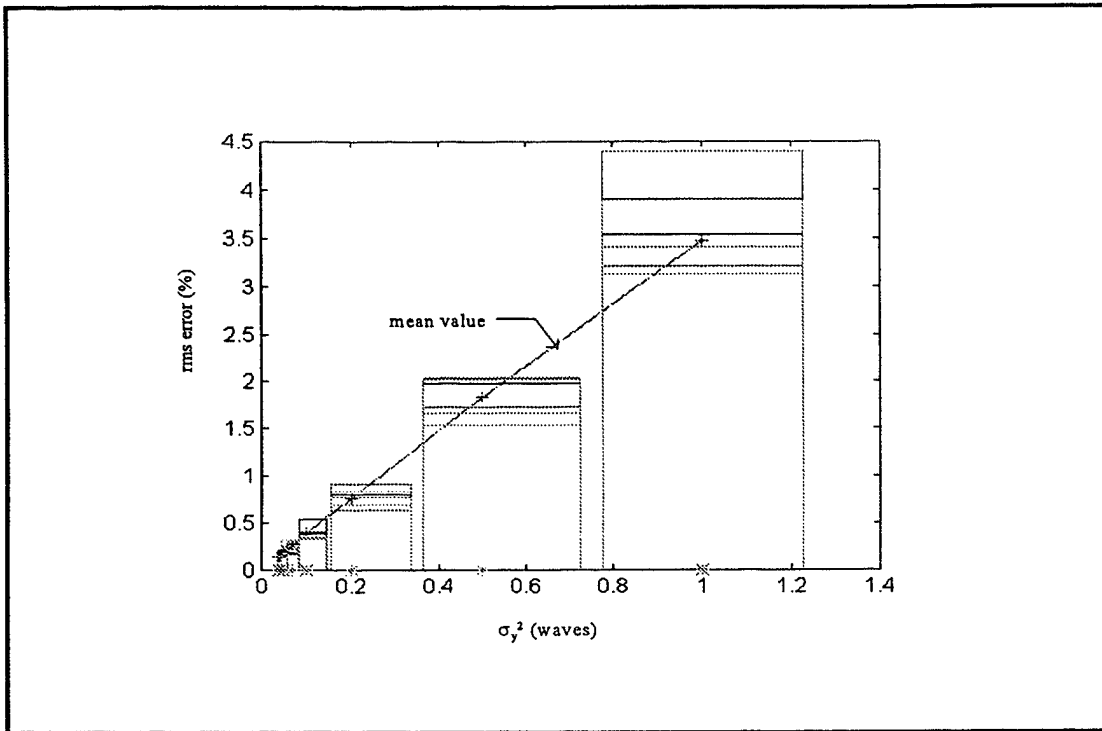


Figure 7 Histogram of RMS beam error versus surface amplitude variations in the y -direction.

The RMS error versus surface height is nearly linear, with a slope of approximately $3.5\%/ \lambda$.

2.3 Spatial frequency analysis

The previous section showed that surface errors play an important role in determining the field distribution near the beam waist. In this section, a more quantitative analysis is performed. Only scattering effects in the x -direction are studied. Using Fourier analysis, the surface can be thought of as a superposition of various sinusoidal phase gratings at different spatial frequencies f_x and different amplitudes A . The value of $h(x)$ is now given by

$$h(x) = A \cos(2\pi f_x x), \quad (3)$$

and $t(x)$ is again given by Eqn. (1). For this study the five different values of BW were used: $5 \mu\text{m}$, $10 \mu\text{m}$, $20 \mu\text{m}$, $40 \mu\text{m}$ and $80 \mu\text{m}$. The results are shown in Figs. 8-12. Two parameters were studied for each value of BW . First, the ratio of the on-axis peak irradiance for the cosinusoidal surface versus the flat surface is calculated. The square root of this ratio is shown in the upper plots. This ratio is similar to the Strehl ratio used in aberration theory. In the lower plots, the square root of the diffraction efficiency is shown. The diffraction efficiency is computed by integrating the irradiance from the values of $-BW < x < BW$ and normalizing to the total irradiance in the beam. Therefore,

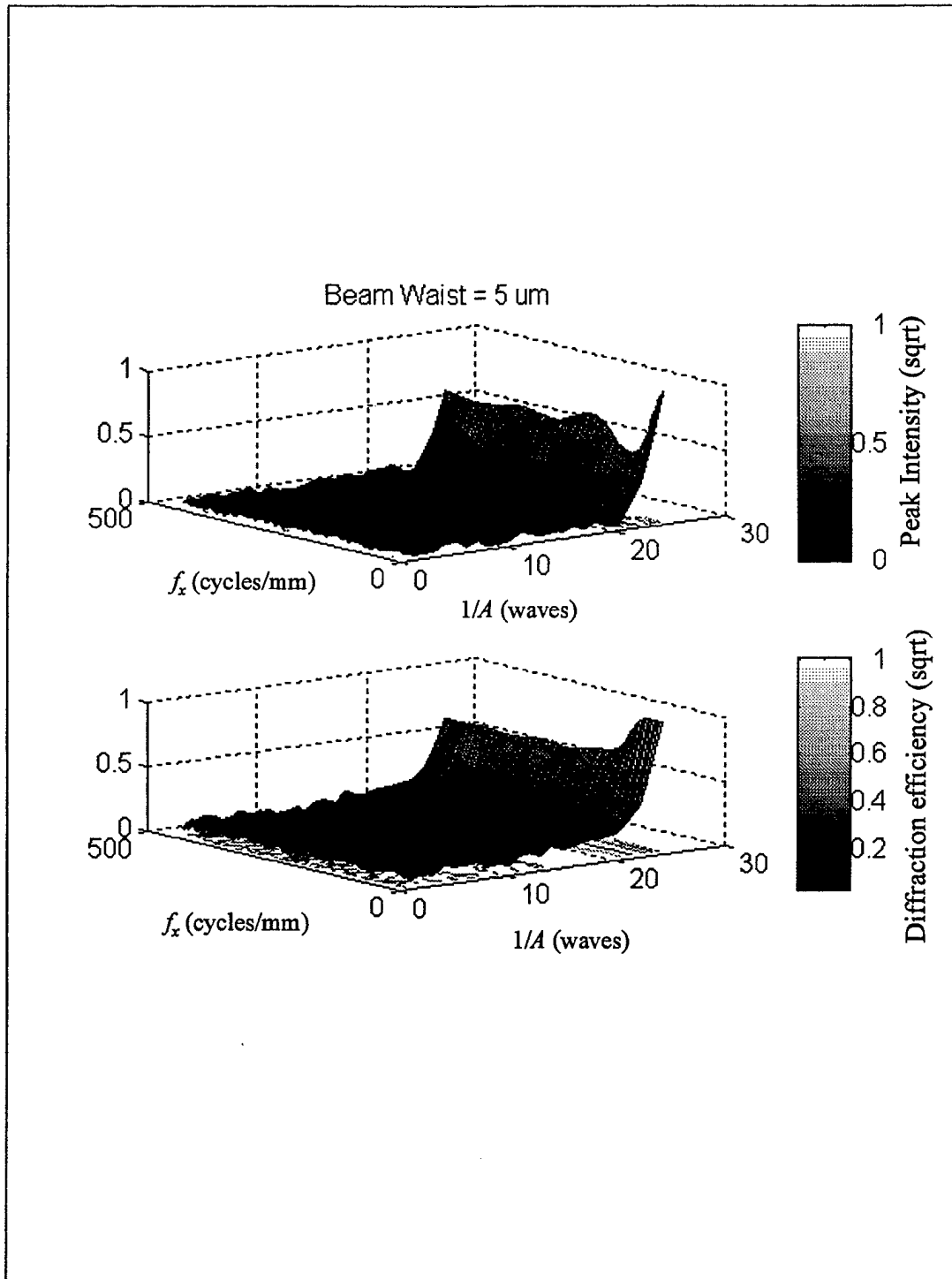


Figure 8 On-axis irradiance fall-off and diffraction efficiency for $BW = 5 \mu\text{m}$.

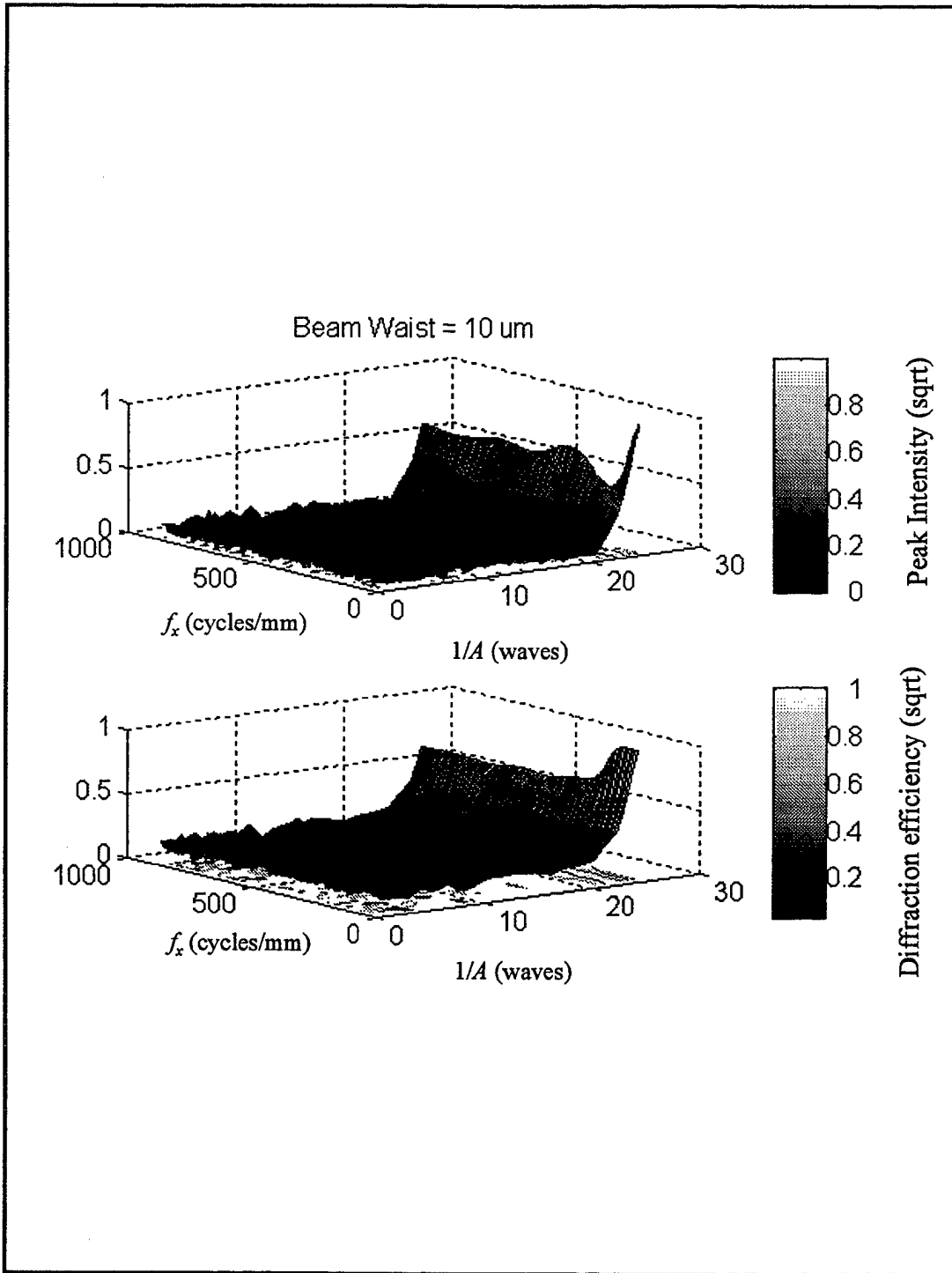


Figure 9 On-axis irradiance fall-off and diffraction efficiency for $BW = 10 \mu\text{m}$.

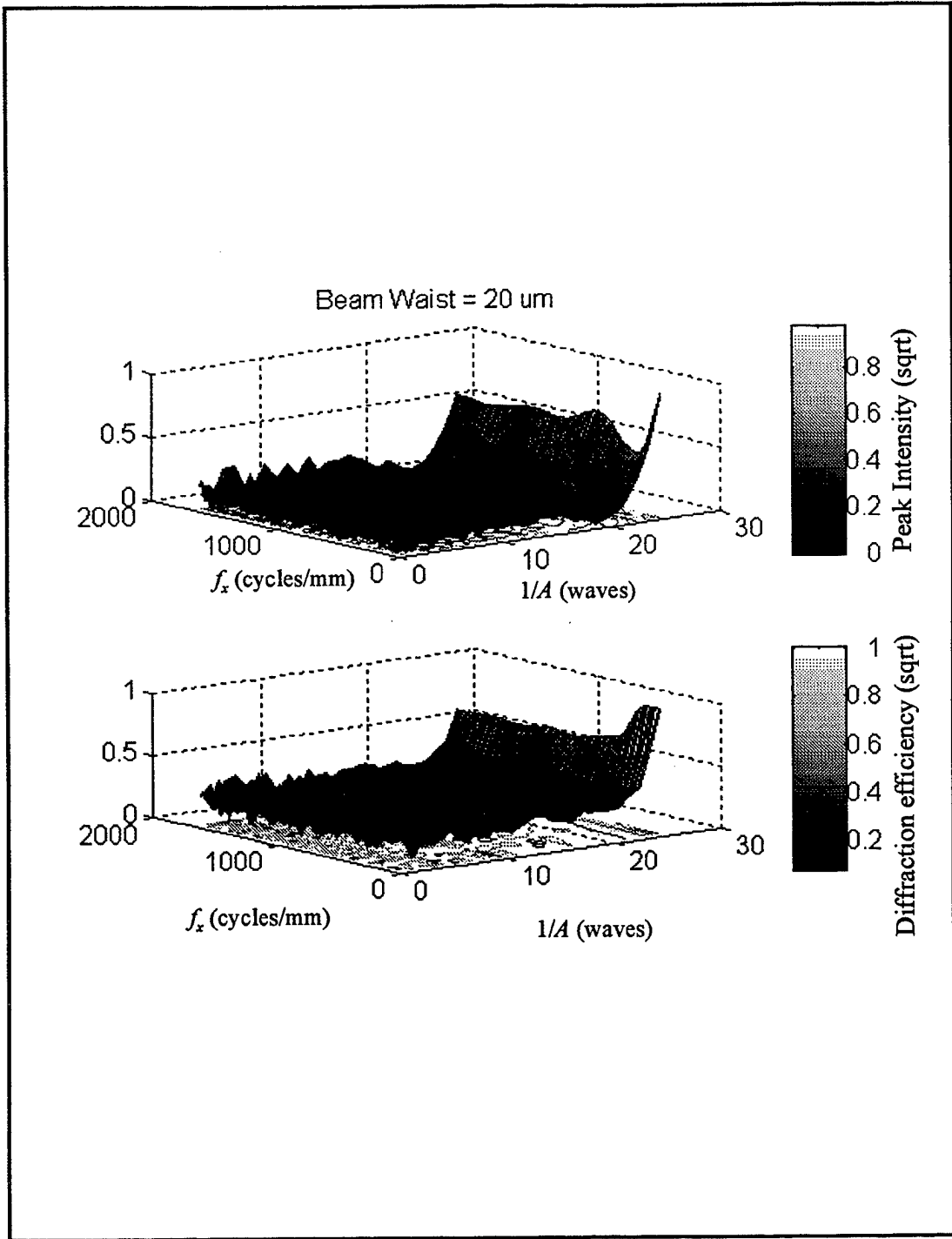


Figure 10 On-axis irradiance fall-off and diffraction efficiency for $BW = 20 \mu\text{m}$.

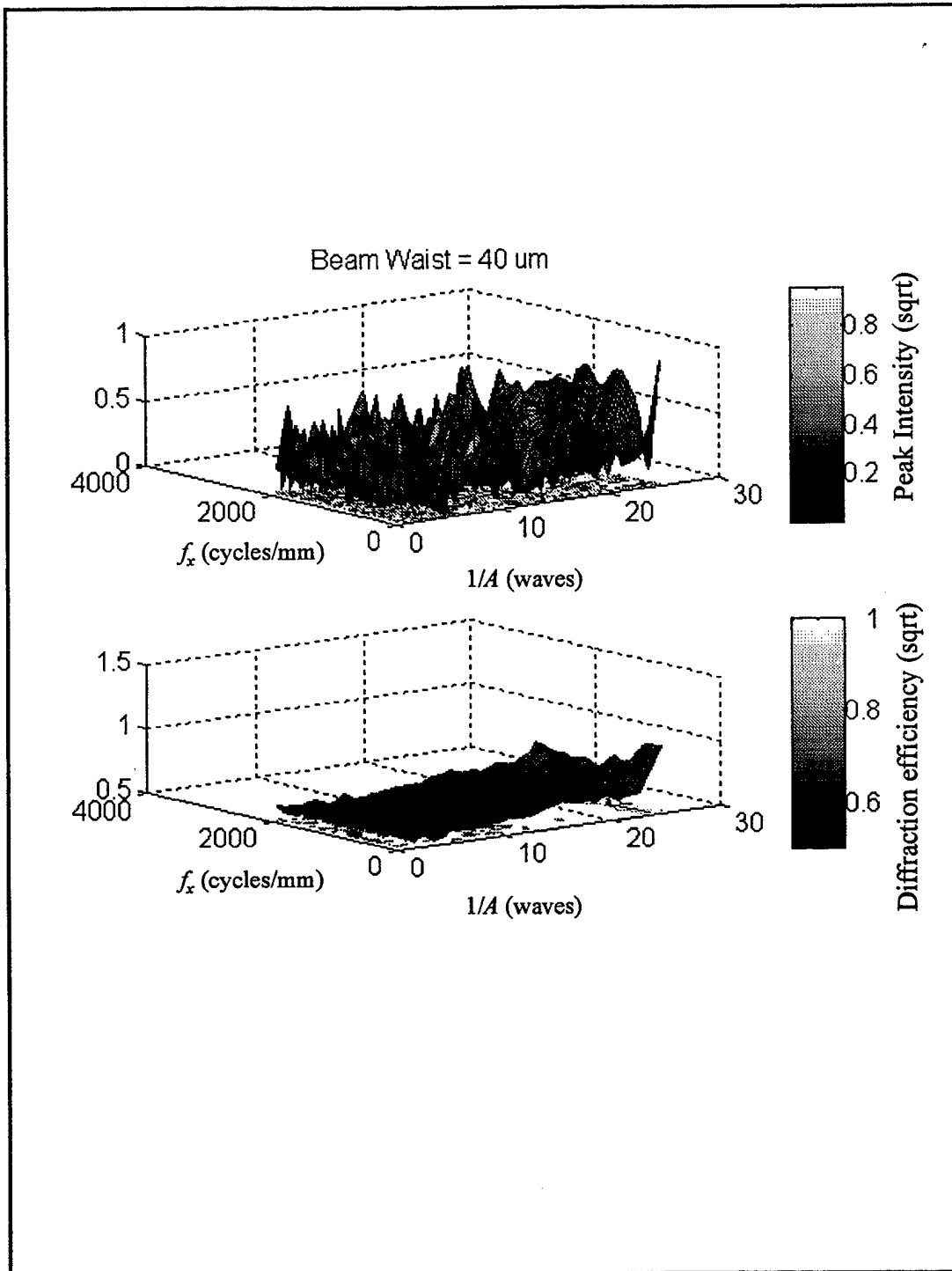


Figure 11 On-axis irradiance fall-off and diffraction efficiency for $BW = 40 \mu\text{m}$.

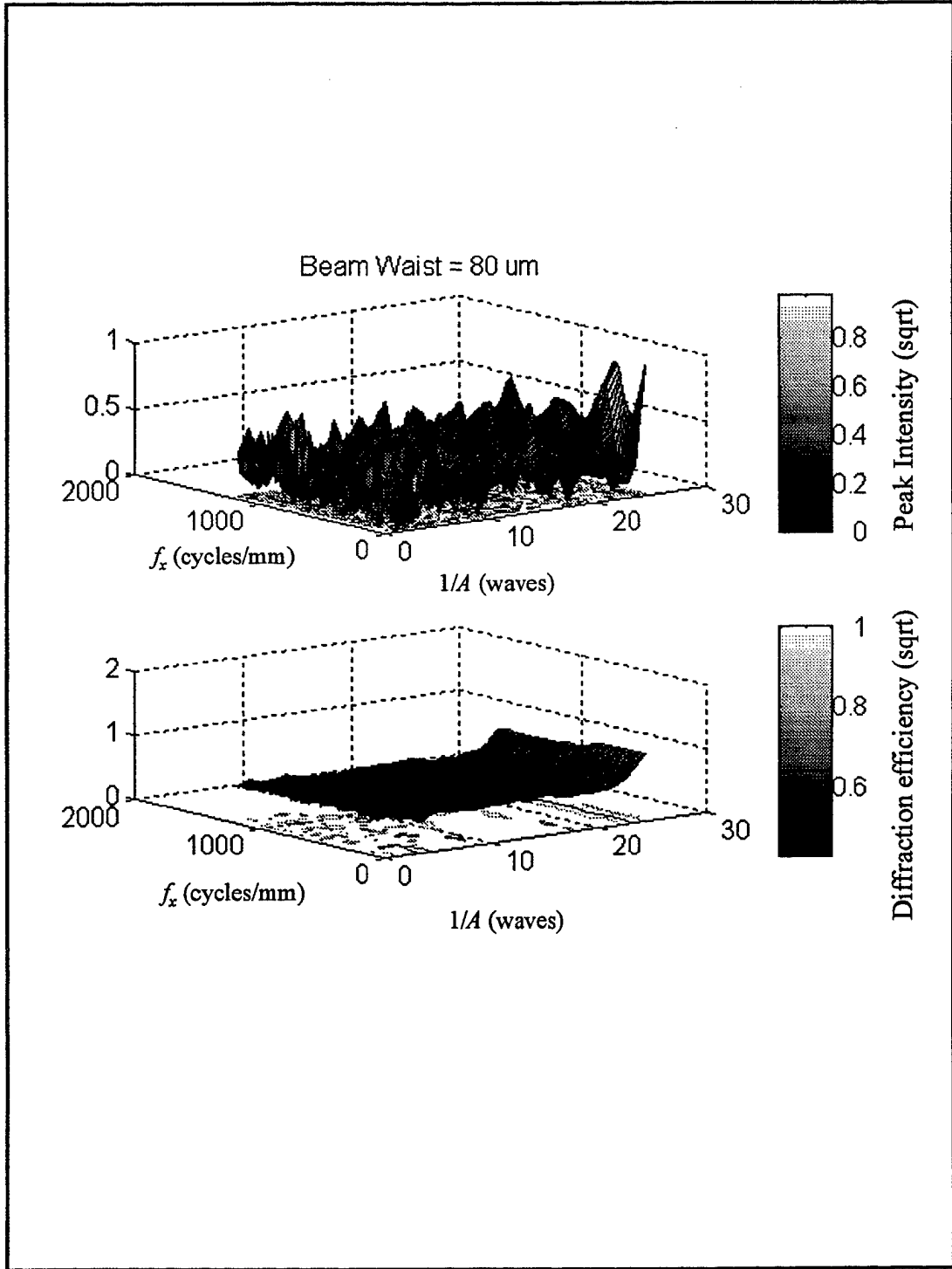


Figure 12 On-axis irradiance fall-off and diffraction efficiency for $BW = 80 \mu\text{m}$.

the diffraction efficiency is a measurement of the percentage of energy transmitted into the central lobe of the beam.

It is apparent that the beam quality degrades quickly for even minimal ($\sim\lambda/10$) surface errors. It is not surprising that the least aberrated spot occurs when the surface varies slowly, and the peak-to-peak amplitude is low. As shown in the previous section, the beam quality is more sensitive to surface variations when the beam print on the front surface is smallest ($BW = 80 \mu\text{m}$).

It is also instructive to plot the field at the waist. Figures 13(a) through (d) and 14(a) through (d) show the field at the waist for values of $A = \lambda/25, \lambda/10, \lambda/5$ and $\lambda/2$, respectively. The solid line corresponds to the beam passing through a flat surface, while the broken line is for the case of a cosinusoidal surface. In Figs. 14(a) through (d), BW is $20 \mu\text{m}$ and f_x is 100 cycles/mm. In Figs. 14(a) through (d), BW is $80 \mu\text{m}$ and f_x is 10 cycles/mm. (There is no particular significance to these values.)

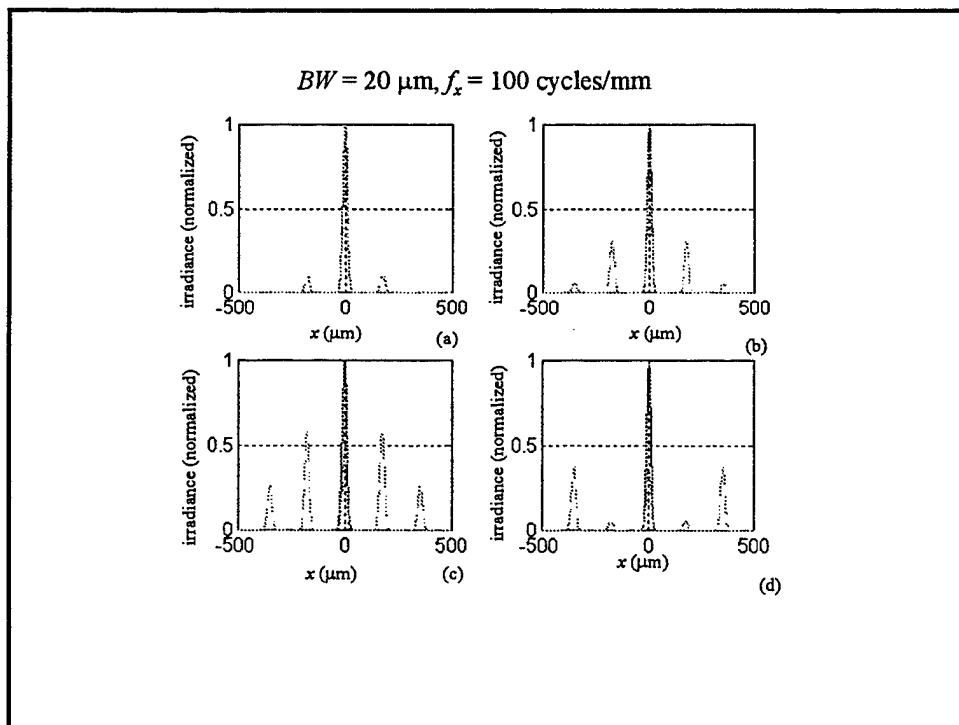


Figure 13 Field profile at beam waist when scattered off of a cosinusoidal phase grating. For this case $BW = 20 \mu\text{m}$ and $f_x = 100$ cycles/mm.

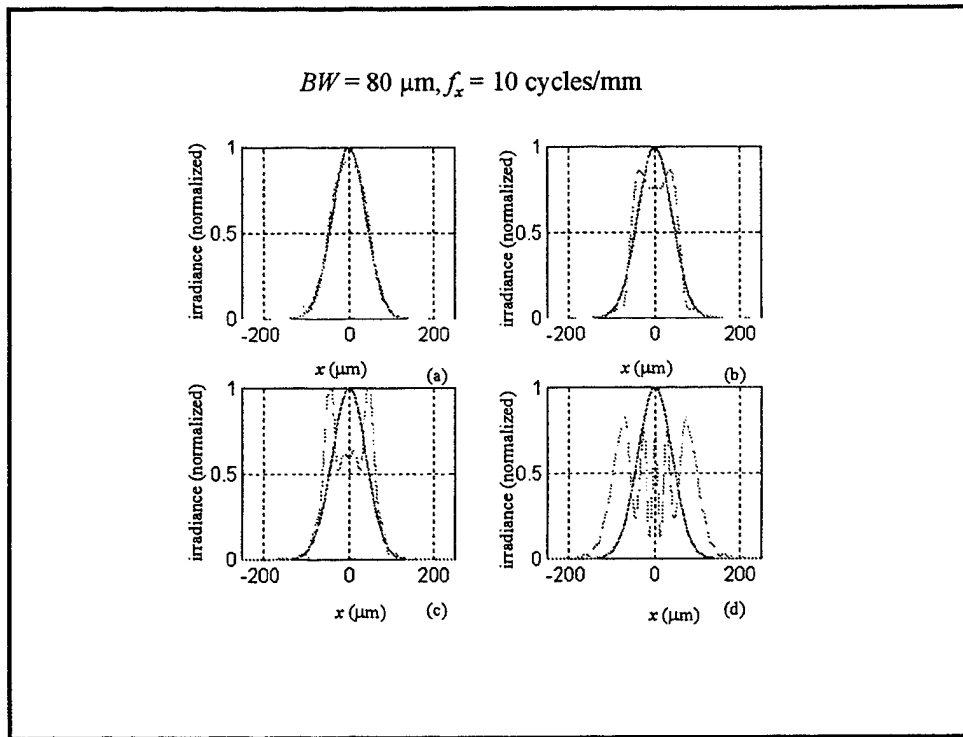


Figure 14 Field profile at beam waist when scattered off of a cosinusoidal phase grating. For this case $BW = 80 \mu\text{m}$ and $f_x = 10 \text{ cycles/mm}$.

Unlike a cosinusoidal amplitude grating, a cosinusoidal phase grating exhibits many diffraction orders. In Fig. 13, the diffraction orders are widely separated. Within the central lobe of the beam the only apparent effect is a loss in amplitude. In Fig. 14, however, the orders are not as widely separated and there are large oscillations within the central lobe. These oscillations result from interference fringes between the different diffraction orders. It is important to point out that all these models assume a perfectly coherent beam. By reducing the coherence length of the beam, the interference fringes would be less severe, and it is expected that the observed oscillations will be reduced. It is important that the beam's coherence be reduced in a method that does not reduce the overall optical throughput of the system. Otherwise, writing times may increase. This is an area of on-going research.

3.0 Scattering from previously written data marks

Another principle area of concern is the effects of scattering within the SP cube as the beam propagates. The scattering may be due to imperfections in the material itself. However, a more likely cause is index variations (both in the real and imaginary part) which are caused by previously written data marks in the material. As the beam propagates through previously recorded planes (pages) of data it is scattered from local index variations induced by the molecular transition which occurs during the writing process. Propagation through hundreds of planes of data, may result in severe perturbations on the beam's spatial properties. Because of this, the noise floor of the recorded data may increase. In addition, the read process may suffer due to readout with aberrated beams. Unfortunately, proper analysis of this problem requires a rigorous, vector-based technique, due to the small spatial dimensions of the data marks (on the order of a few wavelengths). In this section, a rigorous-vector based numerical method is used to analyze the effects of scattering from previously written data pages.

3.1 Numerical model

In Fig. 15(a), the physical setup of the problem is shown. A beam is focused through the SP cube, propagating through randomly written pages of data. To simulate this, a hybrid angular-spectrum/FDTD method is used [7]. The complex-valued field is taken at the exit pupil of the system ($NA = 0.6$), as shown in Fig. 15(b). The model is capable of including optical aberrations, but for this report only unaberrated beams are studied. The field is first propagated to a plane 10-20 μm from focus. During this propagation, the index of refraction is assumed to be the unwritten index of refraction (n_{uw}). At this plane the field is sampled (amplitude and phase), and written to an output file. The complex-valued field is then used in a two-dimensional FDTD program to solve for the steady-state electromagnetic energy distribution in the focal region. Within this region, randomly written data marks exist. The FDTD code is written in FORTRAN and runs on a SPARC 20 workstation. The data marks are assumed to be supergaussian in shape ($n = 4$), with a full-width at half-maximum (FWHM) of 1 μm in the x -direction and a plane-to-plane spacing of 1 μm in the z -direction. Within these marks, the peak index of refraction is denoted by n_w . To simulate the absorption of the material, the proper conductivity, σ_w is used (the conductivity for the unwritten material is assumed to be zero). As a benchmark, the FDTD code is also run when no data marks are present. The difference between these two cases is used to study the effects of scattering.

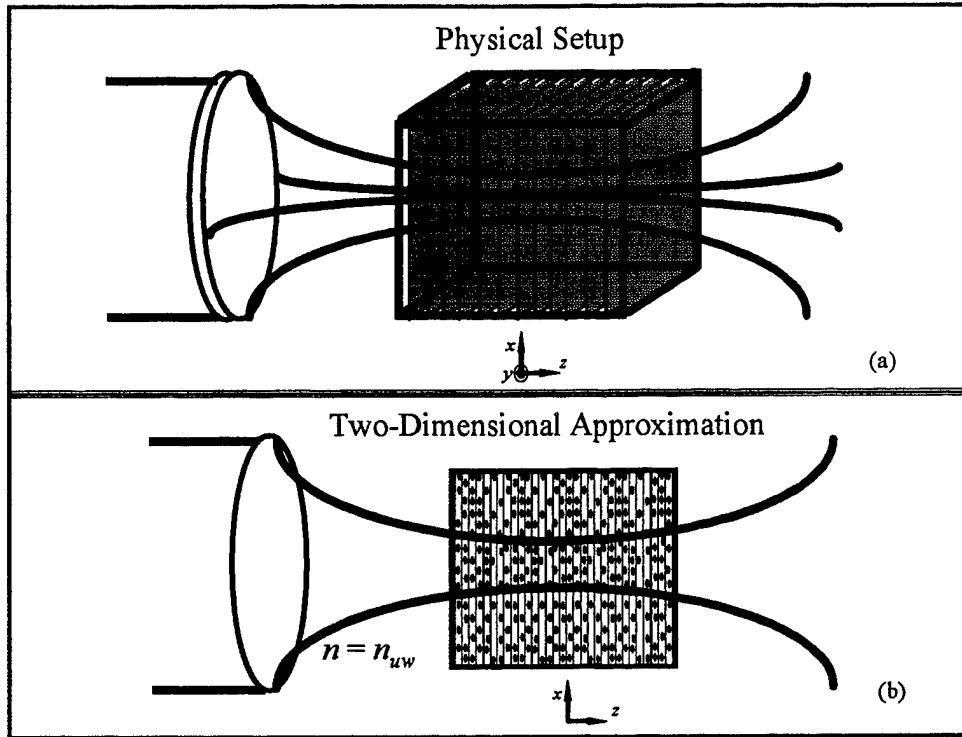


Figure 15 Physical setup (a) and setup of two-dimensional model (b).

For this work, only TE-polarization ($\mathbf{E} = E_y$) is used. In addition, an index difference ($|n_w - n_{uw}|$) of four times that of the SP material is used. This is done to enhance the scattering effects. Because of this, the results presented below are an exaggeration of what is expected in the material currently used by Call/Recall.

3.2 Results

In Figs. 16 through 18 computed results are presented. In Fig. 16, the steady-state value of $|\mathbf{E}|^{1/2}$ is shown. The square root of $|\mathbf{E}|$ is shown to enhance the contrast between features in the main lobe of the beam versus those in the side lobes. In Fig. 17, the phase of \mathbf{E} is shown. Finally, in Fig. 18, a snap-shot in time of the field, after 150 optical cycles, is shown. In each of these plots, the nominal field (no data marks) is plotted in (a), the randomly chosen bit pattern is shown in (b), the field with data marks is shown in (c), and the difference between (a) and (c) is shown in (d). In (d), contours of the data marks are also shown. Also in (b), black areas correspond to written regions of data, while white regions correspond to unwritten regions. For all cases, the focal plane is at $z = 10 \mu\text{m}$.

The results are very interesting. In Fig. 18(d), the difference of the two waves indicates that the major error is not purely random, but a largely deterministic focal shift resulting in a diverging wave. Further analysis shows that the RMS error between the focused spots with written and unwritten data is approximately of 0.6% when the index change is that of SP, 2.7% when the index change is four times that of SP, and 7.5% when the index change is ten times larger than the change in SP. It appears that the defocusing observed

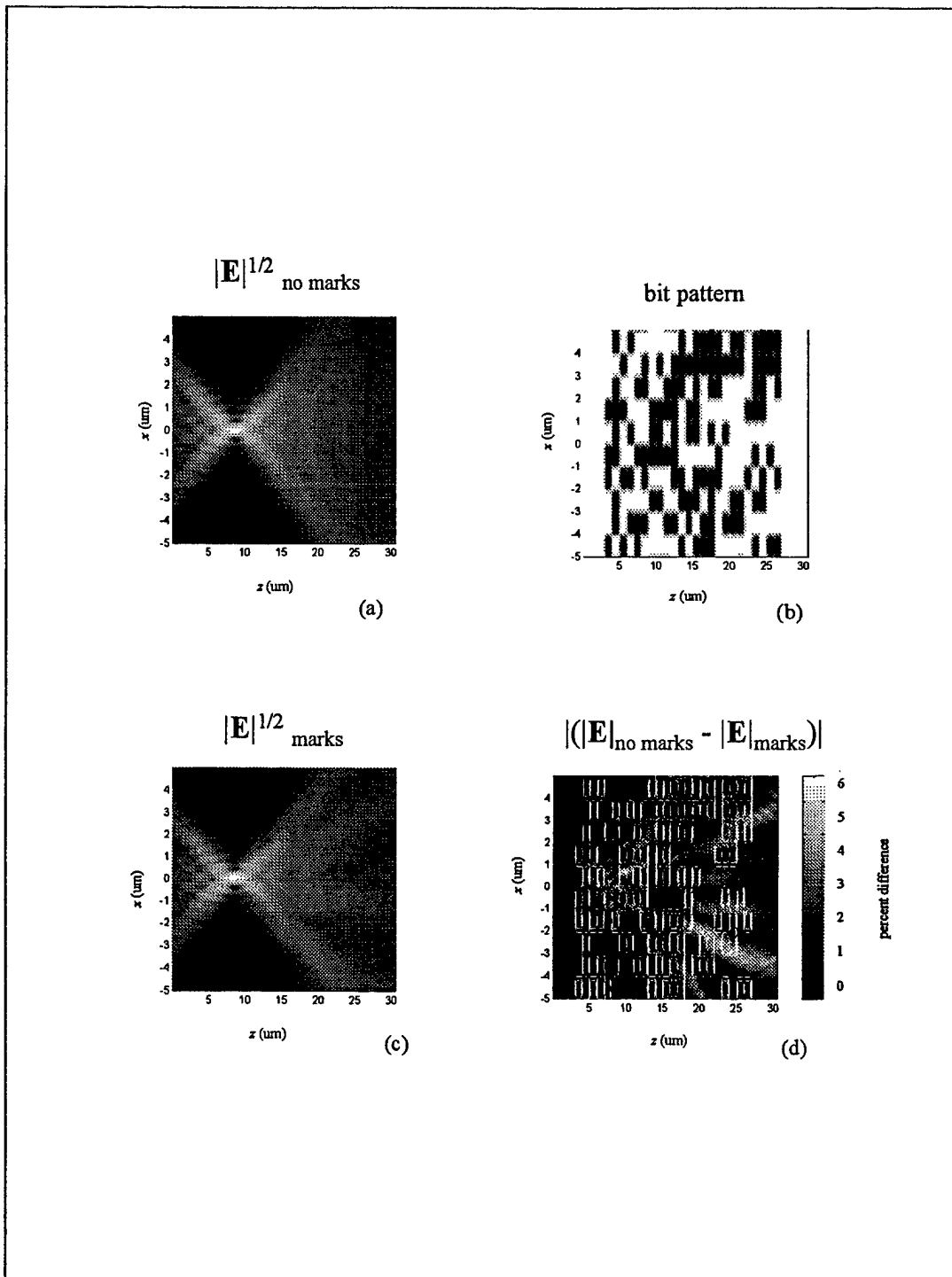


Figure 16 x-z profiles of $|E|$ near-focus.

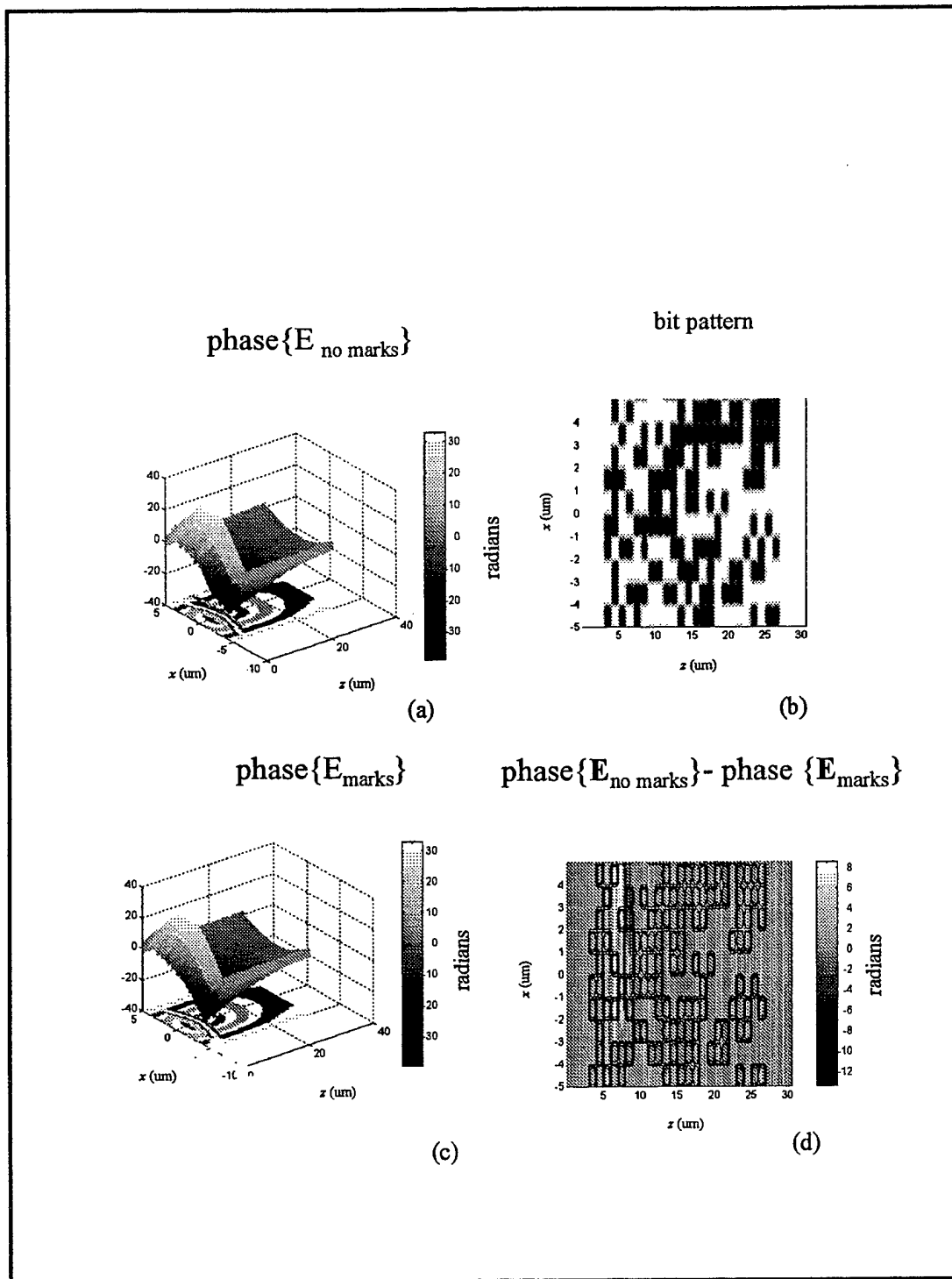


Figure 17 x-z profiles of phase $\{E\}$ near-focus.

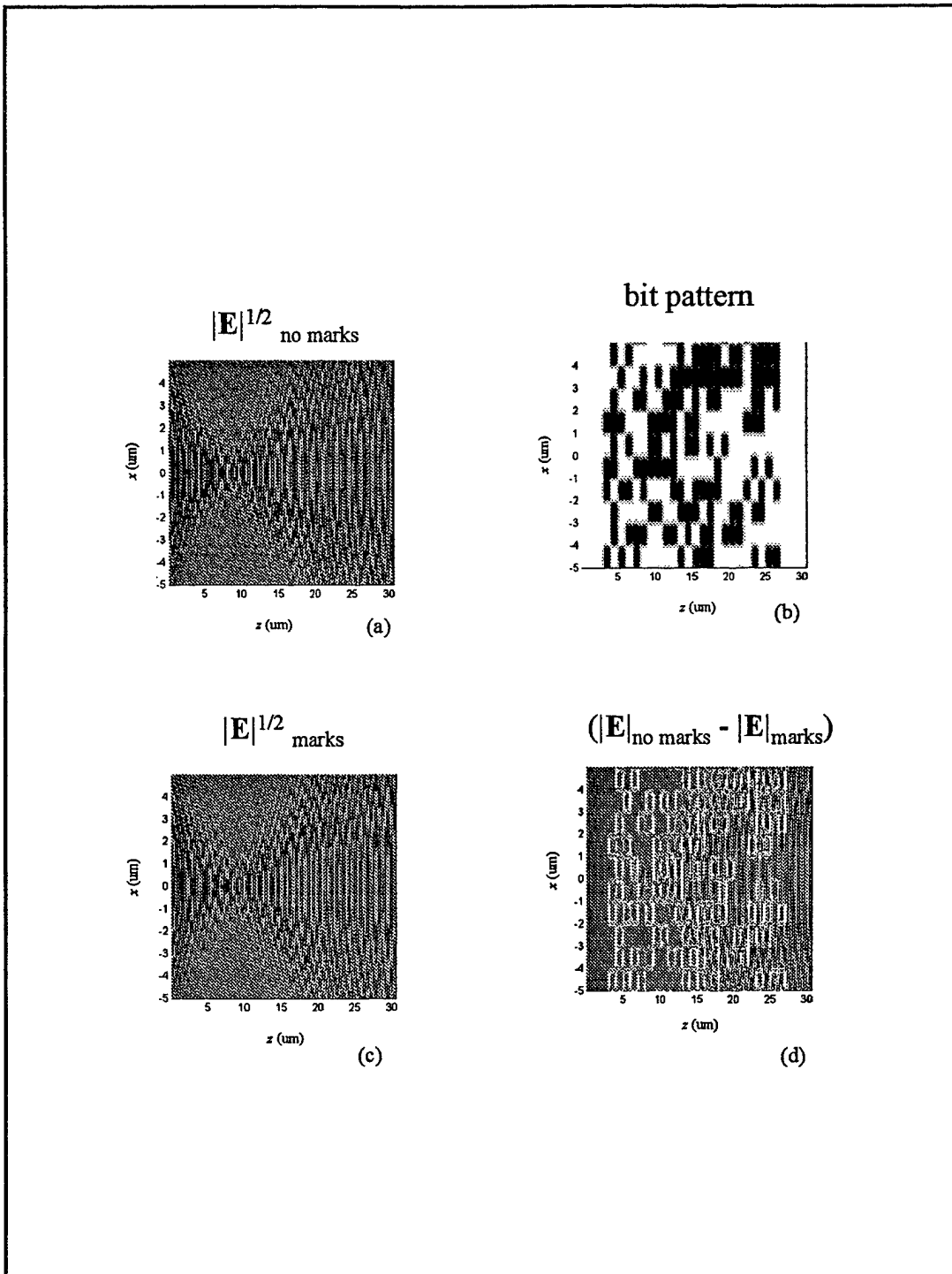


Figure 18 Snapshot in time of x - z profiles of E near-focus. The snapshot is taken after 150 optical cycles.

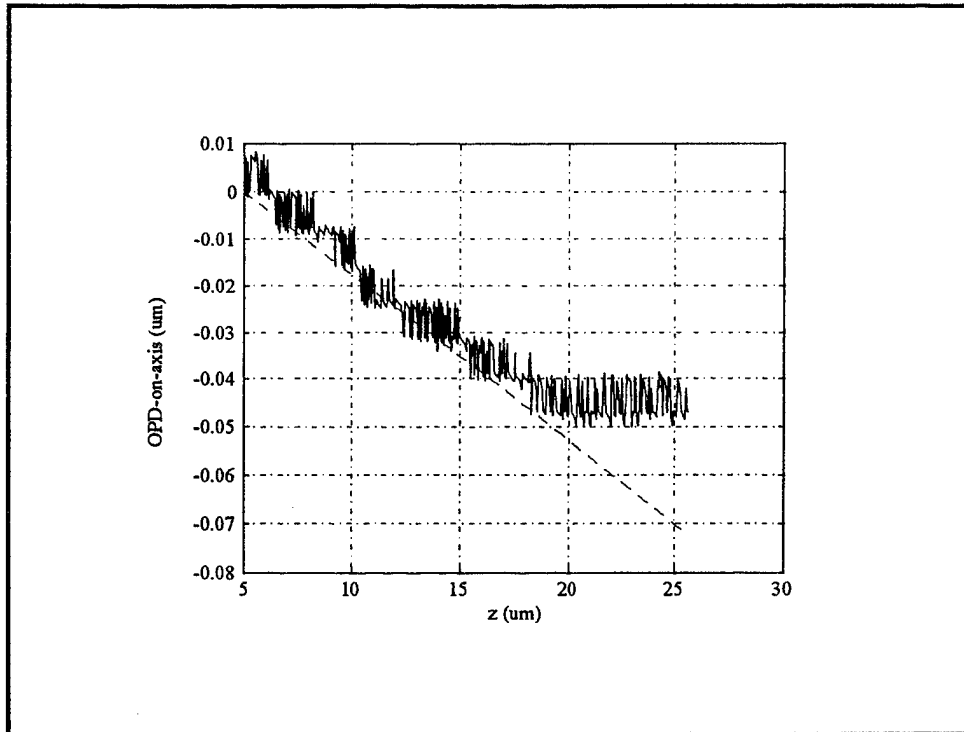


Figure 19 Computed OPD using FDTD/angular spectrum model (solid line) and a simple theoretical model (broken line).

in Fig. 18(d) indicates that the beam propagating through randomly written data planes sees a nominal index of refraction which is slightly different than that propagating through unwritten regions. To show this the Optical Path Difference (OPD) between the two cases is shown in Fig 19. The OPD is found by differencing the on-axis phase terms (piston error), and dividing by k . The results are shown as the solid line. A simple theoretical model is also used, and the results are shown as the broken line. This model assumes a nominal index of refraction for the written case equal to the average value of n_w and n_{uw} .

Very nice agreement is observed between the two cases. Of course, this is done over a very limited range of z . To better simulate this effect, propagation through hundreds of planes of data should be analyzed. Direct application of the FDTD/angular spectrum approach, unfortunately, requires far-greater computing power. Alternative approaches, including a sliding FDTD window, are currently being investigated. It should also be pointed out that this nominal index change will effect the nominal NA of the system and possibly the amount of optical aberrations in the system, specifically spherical aberration. However, the largely non-random portion of these effects is correctable by providing slight active adjustments to the optical system.

4.0 Summary and Conclusions

It has been shown that both surface and bulk scattering plays a significant role in designing a three-dimensional optical memory system. Surface scattering leads to fairly large perturbations in both the quality and centroid position of the addressing beam. In the focused direction, the error is greater for a beam whose width is smaller at the cube's entrance face. In the collimated direction, a nearly-linear relationship exists between the RMS beam error and the magnitude of the surface roughness. Two possible solutions for minimizing surface roughness effects are (a) transitioning to an injection molding process to reduce the roughness and/or (b) reducing the spatial coherence of the beam. This will reduce interference effects from the multiple diffraction orders scattered from the surface.

Propagation through random data marks also plays an important role in the spatial properties of the beam. It has been shown that the amount of random noise is fairly small. It is important to point out that the simulations presented here are somewhat limited for analyzing random noise because of the limited z-range. However, the modeling in this report clearly indicates that by introducing previously recorded pages of data, the beam can be viewed as propagating through a nominal index of refraction that is roughly equal to the average of the written and unwritten indices of the material. The errors induced by this index change can be largely compensated for by providing active control of the optical system. While the index change is fairly small in SP, it will probably be more significant in other multi-layer technologies such as DVD.

5.0 References

1. Jamberdino, A.A., Haritatos, F.N. and Canfield, B.W., "Optical Memories for Large Database Storage," Rome Laboratory Technical Journal, **1**, 81-96 (1995).
2. SONY World Wide Web page detailing DVD specifications and parameters, HTML address, "<http://www.sel.sony.com/SEL/consumer/dvd/specs.html>," (1997).
- * 3. Esener, S. and Rentzepis, P., "Two-Photon 3-D Memories," RL-TR-95-76 Final Technical Report (1995), Dist. auth to US Gov't agencies only.
4. Esener, S., Fainman, Y., Ford, J.E., and Hunter, S., "Two-Photon Three-Dimensional Memory Hierarchy," (Photonics for Computers, Neural Networks and Memories, San Diego CA, 22-24 July 1992), Proceedings of the SPIE-The International Society for Optical Engineering 1993, **1773**, 346-355, (1993).
5. Dvornikov, A.S., and Rentzepis, P.M., "Two-Photon 3-D Optical Memory," IEEE Proc. of 1994 Conference on Solid State Memory Tech., 109-118, (1994).
6. Gaskill, J.D., *Linear Systems, Fourier Transforms, and Optics*, John Wiley & Sons, New York, 1978.
7. Kann, J.L., Milster, T.D., Froehlich, F., Ziolkowski, R.W., and Judkins, J., "Near-field optical detection of asperities in dielectric surfaces", J. Opt. Soc. Am. A. **12**, 501-512 (1995).

***MISSION
OF
ROME LABORATORY***

Mission. The mission of Rome Laboratory is to advance the science and technologies of command, control, communications and intelligence and to transition them into systems to meet customer needs. To achieve this, Rome Lab:

- a. Conducts vigorous research, development and test programs in all applicable technologies;
- b. Transitions technology to current and future systems to improve operational capability, readiness, and supportability;
- c. Provides a full range of technical support to Air Force Material Command product centers and other Air Force organizations;
- d. Promotes transfer of technology to the private sector;
- e. Maintains leading edge technological expertise in the areas of surveillance, communications, command and control, intelligence, reliability science, electro-magnetic technology, photonics, signal processing, and computational science.

The thrust areas of technical competence include: Surveillance, Communications, Command and Control, Intelligence, Signal Processing, Computer Science and Technology, Electromagnetic Technology, Photonics and Reliability Sciences.